

Modeling the Formation of Clouds in Brown Dwarf Atmospheres

Curtis S. Cooper¹, David Sudarsky², John A. Milsom³, Jonathan I. Lunine¹, Adam Burrows²

ABSTRACT

Because the opacity of clouds in substellar mass object (SMO) atmospheres depends on the composition and distribution of particle sizes within the cloud, a credible cloud model is essential for accurately modeling SMO spectra and colors. We present a one-dimensional model of cloud particle formation and subsequent growth based on a consideration of basic cloud microphysics. We apply this microphysical cloud model to a set of synthetic brown dwarf atmospheres spanning a broad range of surface gravities and effective temperatures ($g_{\text{surf}} = 1.78 \times 10^3 - 3 \times 10^5 \text{ cm s}^{-2}$ and $T_{\text{eff}} = 600 - 1600 \text{ K}$) to obtain plausible particle sizes for several abundant species (Fe, Mg_2SiO_4 , and $\text{Ca}_2\text{Al}_2\text{SiO}_7$). At the base of the clouds, where the particles are largest, the particle sizes thus computed range from $\sim 5 \mu\text{m}$ to over $300 \mu\text{m}$ in radius over the full range of atmospheric conditions considered. We show that average particle sizes decrease significantly with increasing brown dwarf surface gravity. We also find that brown dwarfs with higher effective temperatures have characteristically larger cloud particles than those with lower effective temperatures. We therefore conclude that it is unrealistic when modeling SMO spectra to apply a single particle size distribution to the entire class of objects.

Subject headings: atmospheres: clouds, condensation, grains: fundamental parameters — stars: low mass, brown dwarfs, substellar mass objects, L dwarfs, T dwarfs, spectroscopy, atmospheres, spectral synthesis

1. Introduction

Substellar mass objects (SMOs) are fundamentally more complex than Sun-like stars because of the formation of molecules in their cool outer layers. These molecular species cause the spectra to deviate strongly from blackbody values in a multitude of spectral bands (Leggett et al. 1999; Kirkpatrick et al. 1999; Burrows et al. 1997, and references therein). Because of the complex chemistry occurring in their atmospheres, therefore, a comprehensive theory of SMOs requires detailed knowledge of the opacities of all the abundant

molecular species. Obtaining complete opacity data has been a major challenge for the field of SMO spectral synthesis (Burrows et al. 2001).

The chemistry of brown dwarf and giant planet atmospheres is further complicated by the condensation of gaseous molecules into liquid or solid cloud particles, a process which occurs naturally at low temperatures. Because clouds significantly affect spectral features, a satisfactory theory for the structure of substellar atmospheres must address cloud particle formation and subsequent growth. Detailed knowledge of the distribution of particle sizes near the photosphere is a basic requirement for properly modeling the optical effects of clouds (Lunine et al. 1989; Ackerman & Marley 2001).

Clouds influence brown dwarf and giant planet spectra in several important ways. First, cloud formation can deplete the atmosphere of refractory elements that become sequestered in condensed form and then rain out from the upper

¹Department of Planetary Sciences and Lunar and Planetary Laboratory, The University of Arizona, Tucson, AZ 85721; curtis@lpl.arizona.edu, jlunine@lpl.arizona.edu

²Department of Astronomy and Steward Observatory, The University of Arizona, Tucson, AZ 85721; burrows@jupiter.as.arizona.edu, sudarsky@as.arizona.edu

³Department of Physics, The University of Arizona, Tucson, AZ 85721; milsom@physics.arizona.edu

atmosphere. This effect is hypothesized to be important for the interpretation of the L to T dwarf spectral transition (Burrows & Sharp 1999; Burrows et al. 2001). Second, clouds near the photosphere will have the general effect of smoothing out prominent spectral features (Jones & Tsuji 1997). Third, the optical albedo of irradiated objects will be increased substantially by the presence of clouds (Sudarsky et al. 2000). Fourth, the presence of an optically thick cloud layer causes a back-warming effect that results in heating of the atmosphere.

Clouds may be manifest in brown dwarf spectra in a more subtle way. Bailer-Jones & Mundt (2001) reported photometric I-band variability of up to 7% in L dwarf spectra. The effect is a possible signature of variations due to the patchiness of clouds. Unfortunately, cloud patchiness in SMOs is not well understood because even though much is known about the dynamic meteorology of the Earth, these gaseous bodies are dynamically very different. For example, general circulation models of the Earth, although they are of great utility for studying Mars, completely fail to reproduce the observed dynamics in Jupiter’s atmosphere. A detailed, three-dimensional cloud model paralleling the state of the art in Earth climate models would require detailed meteorological measurements for proper parameter calibration that are simply not available for any other planet.

The present cloud model at its core employs the basic microphysical timescale arguments of Rossow (1978) to determine the most probable particle size in a cloud at each vertical pressure level. The model is one-dimensional only. We make no attempt to treat the intricacies of cloud patchiness or the effects of winds and horizontal advection. The present cloud model is not intended to calculate the detailed meteorology of planetary atmospheres but to offer a simple prescription for estimating the opacity of clouds in SMO atmospheres. A detailed but computationally cumbersome SMO climate model, if it could be developed, would be difficult to incorporate into spectral synthesis models. The philosophy behind a simple, one-dimensional approach to cloud modeling is to develop a prescription based on well-established physical principles that can be used to guide and inform spectral synthesis calculations. The present model aims to characterize

SMO cloud particle sizes and densities in a global and time averaged sense. We therefore assume the particle number density of the cloud to be uniform across the spherical surface of an object at a given pressure and temperature, and that there has been sufficient time in these systems to establish chemical equilibrium throughout the atmosphere.

Our timescale arguments compute an average effectiveness for each of the various competing physical processes. Therefore, the output particle sizes clearly depend directly on our assumptions of the values of the four unknown parameters in the microphysical timescales (see Section 2.3). The calculation represents a first-order estimate of SMO cloud particle sizes, and we therefore present our results for SMO particle sizes with the realization that the procedure employed could potentially overestimate or underestimate the true particle sizes by some unknown factor, which we expect will be of order unity. Nevertheless, since we have been consistent in the assumed values of the unknown physical parameters throughout the calculation, we expect that the errors in the computed particle sizes will be uniform among the SMOs studied. We are therefore confident, despite the inaccuracies of the approach, that the sizes computed are correct to within an order of magnitude and that the *trends* we demonstrate, in which typical cloud particle sizes vary systematically with brown dwarf effective temperature and gravity, do represent physically meaningful results.

In this paper, we reiterate the general conclusion arrived at in Lunine et al. (1989) and Ackerman & Marley (2001): it is not satisfactory when modeling brown dwarf spectra to assume *a priori* a single particle size distribution because the sizes of cloud particles vary strongly with effective temperature, surface gravity, and height in the atmosphere. We extend the previous efforts to incorporate clouds into spectral models by calculating particle sizes based on a one-dimensional model of cloud particle growth for several abundant species over a range of realistic atmospheric conditions. We compute particle radii spanning a broad range from about $5\ \mu\text{m}$ to over $300\ \mu\text{m}$. Therefore, in the context of this discussion, we hereafter refer to particles less than $10\ \mu\text{m}$ in radius as small; we refer to particles in the range from $10 - 100\ \mu\text{m}$ in radius as medium-sized; and we consider large particles to be those having radii

greater than $100\ \mu\text{m}$.

In Section 2, we present an improved model of cloud formation and droplet growth to determine the composition, abundance, and distribution of cloud particles in brown dwarf atmospheres. In Section 3, we obtain modal cloud particle sizes for several representative cloud-forming species of high abundance for atmospheric models spanning a broad range of effective temperatures and surface gravities. In Section 4, we compare our particle sizes with those of two other recent papers that have also addressed clouds (Ackerman & Marley 2001; Helling et al. 2001). In Section 5, we apply our cloud model to brown dwarf spectra by computing the opacity of clouds resulting from the wavelength-dependent effects of Mie scattering and absorption of radiation. We also demonstrate the importance of clouds as an opacity source by comparing the spectrum of a cloudy brown dwarf atmosphere with that of a cloud-free atmosphere.

2. The Cloud Model

2.1. Condensation Level

The present cloud model follows much of the formalism of Lewis (1969), Rossow (1978), Stevenson & Lunine (1988), and Lunine et al. (1989). To aid the reader, we list in Table 1 all the symbols used in our cloud model as described in this section of the text.

As in Lewis (1969), we compare the partial pressure of a given condensable species to its saturation vapor pressure. Only at levels where the partial pressure exceeds the saturation vapor pressure can condensation begin. However, the required level of supersaturation for efficient condensation depends on the physics of the nucleation process itself. We discuss the two relevant nucleation processes—homogeneous and heterogeneous nucleation—in more detail in Section 2.2. In a clean atmosphere, in which the availability of condensation nuclei is low (the case of homogeneous nucleation), condensation will not begin until the vapor becomes highly supersaturated. Thus, the partial pressure will greatly exceed—often by a factor of two or more—the saturation vapor pressure (Rogers & Yau 1989). This situation is hypothesized to occur in methane clouds in Titan’s atmosphere (Tokano et al. 2001). The condensa-

tion level appears where

$$P_{\text{cond}} > P_{\text{sat}} (1 + \mathcal{S}_{\text{max}}). \quad (1)$$

In Equation 1, P_{cond} is the partial pressure of the condensing vapor, and P_{sat} is its saturation vapor pressure. The \mathcal{S}_{max} parameter is the assumed maximum supersaturation. For example, if $\mathcal{S}_{\text{max}} = 0.01$, then the partial pressure of the condensing vapor must be 1% larger than the saturation vapor pressure before condensation can begin. To aid future discussions, we also define the *saturation ratio* as $S = P_{\text{cond}}/P_{\text{sat}}$.

In addition to the original Lewis (1969) cloud model, we also treat the case of heterogeneous (or chemical) condensation, in which chemical constituents different in composition from the cloud react chemically to produce the condensate. For example, we allow Mg, Si, and O to produce forsterite, Mg_2SiO_4 . In such cases of heterogeneous condensation, the concept of a saturation vapor pressure is replaced by the heterogeneous condensation pressure. We apply the chemical equilibrium model of Burrows & Sharp (1999) to a solar-composition gas (Anders & Grevesse 1989) to determine which chemical species are thermodynamically favored. The calculation determines the equilibrium compositions by minimizing the Gibbs free energy of the system.

The maximum supersaturation, \mathcal{S}_{max} in Equation 1, appears in the calculation as an essentially free parameter, though we have some guidance as to its likely value from measurements of the supersaturation of water clouds on Earth. We assume in these calculations that the abundance of condensation nuclei is sufficient for heterogeneous nucleation to begin at only 1% maximum supersaturation, though we will explore the effect of this parameter on the computed particle sizes subsequently (see Section 3.4). We have not attempted herein to calculate the precise composition or abundance of these condensation nuclei. But even for iron, which is the most refractory of the homogeneously condensing species, we argue based on chemical equilibrium considerations that there exist abundant refractory condensates that can potentially serve as nucleation sites for heterogeneous nucleation, including corundum (Al_2O_3), hibonite ($\text{CaAl}_{12}\text{O}_{19}$), the calcium titanates (e.g., CaTiO_3 and $\text{Ca}_4\text{Ti}_3\text{O}_{10}$), grossite (CaAl_4O_7) and other calcium-aluminum oxides,

TABLE 1
CLOUD MODEL VARIABLES AND PARAMETERS

Symbol	Description
$g_{\text{surf}}, T_{\text{eff}}$	SMO surface gravity and effective temperature.
$P_{\text{cond}}, P_{\text{sat}}$	Partial pressure of the condensing vapor and its saturation vapor pressure.
S_{max}, S	Assumed maximum supersaturation and the saturation ratio.
$\tau_{\text{cond}}, \tau_{\text{nuc}}$	Timescales for heterogeneous and homogeneous nucleation.
$\tau_{\text{coal}}, \tau_{\text{coag}}$	Timescales for coalescence and coagulation.
$\tau_{\text{fall}}, \tau_{\text{conv}}$	Timescales for gravitational fallout and convective upwelling.
τ_{rad}	Timescale for particles to cool by radiation.
T, P, ρ, η	Temperature, pressure, mass density, and dynamic viscosity of the atmosphere.
R, k_b, N_A	Universal Gas Constant, Boltzmann's Constant, and Avogadro's Number.
μ, μ_p	Mean molecular weight of atmosphere and condensate molecular weight.
Kn, Re	Knudsen and Reynolds numbers.
$\lambda, c_{\text{sound}}$	Mean free path of atmospheric gas particles and atmospheric sound speed.
v	Relative velocity between particle and fluid in Re expression.
$v_{\text{fall}}(r), g$	Terminal velocity of particles of radius r in local acceleration of gravity, g .
v_{conv}	Upward velocity of convecting gas parcels.
H	Atmospheric scale height; i.e., pressure e-folding distance.
$\epsilon_{\text{surf}}, L$	Surface tension of condensed molecules and the latent heat of vaporization.
r_c, Z	Critical radius of particles and the Zeldovich factor of classical nucleation theory.
N	Number density of cloud particles.
$\epsilon_{\text{coal}}, \epsilon_{\text{coag}}$	Coalescence and coagulation efficiencies.
q_c	Moles of condensate per mole of atmosphere.
q_v	Moles of condensable vapor per mole of atmosphere.
q_t	Total moles of condensable material per mole of atmosphere.
q_{below}	Mole fraction of condensable vapor below the cloud base.
$P_{c,1}$	Condensation curves as shown in Figure 1.
$n(r), r_0$	Particle size distribution about modal particle size, r_0 .

and spinel (MgAl_2O_4).

As in Rossow (1978), we ignore variations in \mathcal{S}_{max} within the cloud. Although in reality the supersaturation should decrease with altitude, we ignore this effect in the present calculations. Furthermore, it is possible to have a small amount of condensate present between $S = 1$ and $S = 1 + \mathcal{S}_{\text{max}}$, even though condensate cannot possibly form there (since the initial condensation of vapor into embryonic particles in general requires at least a modest level of supersaturation). However, particles can settle into the region between $S = 1$ and $S = 1 + \mathcal{S}_{\text{max}}$ once they have formed and yet still be thermodynamically stable. Since it depends on a balance between the processes of gravitational settling and convective upwelling, the amount of cloud material present in the barely supersaturated region is difficult to calculate with certainty. The clouds we treat in this article have a very low \mathcal{S}_{max} , and therefore the errors introduced by neglecting these effects are small. In a cloud having very few condensation nuclei, which as we have stated would require a large \mathcal{S}_{max} , considerations such as the variation of the supersaturation with altitude and the exact location of the cloud base become more crucial for accurate cloud modeling. The present cloud model is not configured to account for these effects realistically, though they are relatively unimportant for the low supersaturations generally assumed throughout this paper.

Figure 1 shows the condensation curve for two condensates, forsterite (Mg_2SiO_4) and gehlenite ($\text{Ca}_2\text{Al}_2\text{SiO}_7$), as well as the “effective condensation curve” of iron derived from the iron saturation vapor pressure curve, and several model brown dwarf atmospheres. As the caption to Figure 1 explains, the curve labeled “Fe” is not the true saturation vapor pressure curve of iron. It is an “effective condensation curve” derived by taking the saturation vapor pressure of iron and dividing by the number mixing ratio of iron vapor just below the cloud base (parameter q_{below} of Table 2), which is the maximum allowed number mixing ratio of gaseous iron in a solar composition mixture when hydrogen is all in molecular form (H_2). We discuss this further in Section 2.3.

The intersection points between the four long-dashed curves of brown dwarf temperature–pressure profiles and the condensation curves of forsterite and gehlenite represent levels in the at-

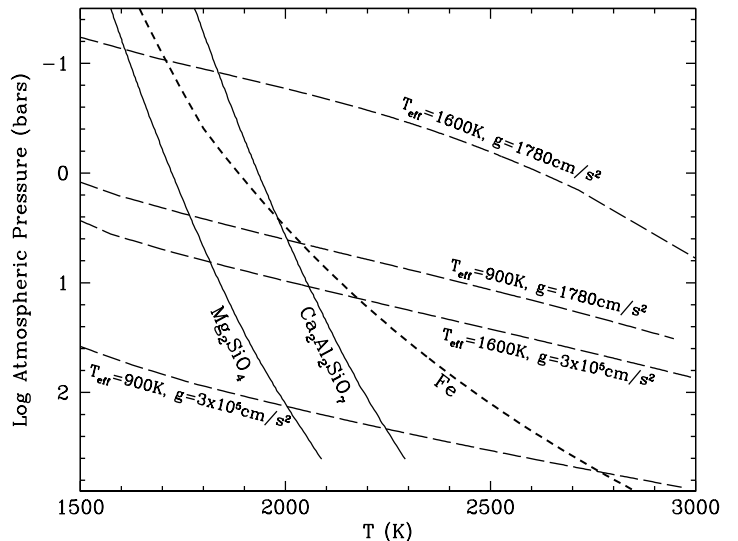


Fig. 1.— Illustrates the locations of the cloud bases for four different atmospheric models (long-dashed curves) and three different chemical species (solid and short-dash curves). The atmospheric models are at two different surface gravities and two different effective temperatures. The short-dashed curve defines the atmospheric pressures and temperatures for which the vapor pressure of iron equals its saturation vapor pressure. This curve is obtained using the iron saturation vapor pressure expression in Barshay & Lewis (1976). The saturation vapor pressure curve has been adjusted using the iron vapor mixing ratio (by number) below the cloud (parameter q_{below} in Table 2). The two solid lines are the curves which illustrate when condensation of forsterite (Mg_2SiO_4) and gehlenite ($\text{Ca}_2\text{Al}_2\text{SiO}_7$) become thermodynamically favored. Thus, they represent the pressure dependent condensation temperatures of those species under the assumption that chemical equilibrium holds. The intersection of a given atmospheric model and the two condensation curves represents the pressures and temperatures at the bases of the chemically condensing clouds in our cloud model. However, for iron, the cloud base will be at lower temperature and pressure than the intersection point if the iron vapor is significantly supersaturated (see Equation 1).

mosphere at which the relevant species may appear via one or more chemical reactions.

The more familiar case of homogeneous condensation, or direct condensation from a vapor of the same composition, does occur for water and iron. Thus, for the condensation of iron and water, we follow Lewis (1969) and employ the well-known saturation vapor pressure relations of iron and water (Barshay & Lewis 1976; Lunine et al. 1989). In Figure 1, the iron curve is thus shown as a thick, short-dashed line as a reminder that the iron cloud condenses directly from iron vapor. As we discuss in more detail in Section 5.3, in which we explore the coupling between clouds and the radiative transfer problem, the atmospheres used in this stage are computed on the basis of an independent, dust-free stellar atmosphere code.

2.2. Microphysical Timescales

Although the chemistry applying to brown dwarf atmospheres is radically different from Earth’s atmospheric chemistry, we nevertheless treat the various competing effects in the cloud formation process as microphysical timescales (Rossow 1978). In our model, five microphysical processes compete with gravitational fallout to increase the modal particle size: 1) convective uplifting of condensable vapor, 2) heterogeneous nucleation, 3) homogeneous nucleation, 4) coagulation, and 5) coalescence. Each process is characterized by a single-valued timescale which expresses its relative importance.

The expressions for four of the microphysical timescales are computed in Rossow (1978): τ_{cond} (heterogeneous condensation), τ_{coal} (coalescence), τ_{coag} (coagulation), and τ_{fall} (gravitational fallout). These expressions depend on the values of both the Knudsen and Reynolds numbers, which characterize how particles of different sizes interact physically with the surrounding fluid and with each other. It is therefore necessary to calculate these values during the particle growth phase of the calculation (see Section 2.3).

We also require an equation of state relating the gas density to its temperature and pressure. In this model, we employ the ideal gas equation of state to relate the gas mass density ρ to the atmospheric temperature and pressure (T, P): $\rho = \mu P / RT$, where R is the universal gas constant,

$8.314 \times 10^7 \text{ ergs mol}^{-1} \text{ K}^{-1}$. The equation of state depends on the mean molecular weight of the atmospheric gas mixture. For these atmospheres, we use $\mu = 2.36 \text{ g mol}^{-1}$, the mean molecular weight of a solar composition gas in which hydrogen is present in the molecular state, H_2 . We have used the chemical equilibrium model of Burrows & Sharp (1999) to verify that—as for Jupiter—molecular hydrogen is the dominant phase of hydrogen in the upper atmospheres of SMOs. The ideal gas equation of state reproduces to within 1% the value of ρ obtained using the more sophisticated thermodynamic equation of state described in Burrows et al. (1989).

The dimensionless Knudsen number differentiates between the two regimes—classical and gas kinetic—of physical interaction between cloud particles and the surrounding medium:

$$\text{Kn} = \lambda / r, \quad (2)$$

where r is the cloud particle’s radius and λ is the mean free path of atmospheric gas particles. The transition between the two regimes occurs where the Knudsen number is near unity (i.e., where $\lambda \sim r$). The high Knudsen number regime, in which the mean free path of gas molecules is much larger than the size of a typical cloud particle, will normally not occur in SMO clouds. However, there are two situations in which large Knudsen numbers could arise: 1) when particles are smaller than $\sim 1 \mu\text{m}$ in radius, and 2) high up in the atmosphere of a planet or brown dwarf at pressures much less a bar. We include the Knudsen number in the cloud model to account for these possibilities.

The dimensionless Reynolds number characterizes the behavior of a spherical particle moving through a fluid. The equation for the Reynolds number is

$$\text{Re} = \frac{2\rho v r}{\eta}, \quad (3)$$

where ρ is the mass density of gas in the atmosphere, r is the radius of the particle, v is the velocity of the particle relative to the fluid, and η is the dynamic viscosity of the fluid. The flow will be turbulent for $\text{Re} \gg 10$ but laminar for low Reynolds numbers (Landau & Lifshitz 1959). For the purposes of these calculations, we assume laminar flow unless $\text{Re} > 70$ (see Section 2.3). This

choice for the laminar to turbulent cutoff is convenient because above $Re = 70$, the drag coefficient describing the variation in terminal velocity of a falling particle becomes roughly a constant at $C_D \approx 0.2$ (Rossow 1978).

To calculate the Reynold’s number and the timescale for gravitational fallout, we introduce an approximate value for η , the dynamic viscosity. The viscosity of a hydrogen and helium gas mixture at low densities is roughly constant over a broad range of temperatures. Because the viscosity increases with the square root of temperature at low pressures, it varies by less than a factor of two over the full range of SMO effective temperatures discussed herein (see Section 2.3). For simplicity, our model therefore assumes a constant value for the dynamic viscosity of $\eta = 2 \cdot 10^{-4}$ poise, which is consistent with the measured values of η for hydrogen and helium at low densities and $T \sim 1000$ K (Lide 1991, CRC Handbook).

The τ_{fall} timescale represents gravitational fallout of particles, which is the fundamental process limiting particle growth. As the particles become large, they fall out. We take the gravitational fallout timescale to be the time required for particles to fall through a pressure scale height of the atmosphere at terminal velocity.

The terminal velocity of falling particles depends on their size, shape, density, rigidity, and the nature of the fluid flow around them (e.g., Stokes flow, free molecular flow, or turbulent flow). We assume rigid spherical particles throughout this paper. While it is true that liquid particles of a given size will fall more slowly through the atmosphere than solid particles because of the disruption of their shape, the effect will not significantly alter the fall speeds for particles smaller than about a millimeter (Rogers & Yau 1989). The particles we obtain using this model—see Section 3—never grow large enough for the difference in terminal velocity between solid and liquid particles to be noticeable. Thus, taking the particles to be rigid spheres is in this case a reasonable simplification.

For the common case of low Knudsen and low Reynolds number flow, the terminal velocity will be given by the Stokes solution for a falling rigid sphere (Rogers & Yau 1989). The Cunningham factor, $1 + \frac{4}{3}Kn$, accounts for the variation in the

terminal velocity with Knudsen number. There is also a variation in terminal velocity with Reynold’s number. These combined effects yield three different forms for the terminal velocity v_{fall} as a function of the radius r of the particle:

$$v_{\text{fall}}(r) = r^2 \cdot \left(\frac{2\rho_{\text{cond}}g}{9\eta} \right) \quad Re < 70, Kn < 1, \quad (4)$$

$$v_{\text{fall}}(r) = r^{1/2} \cdot \sqrt{\frac{40\rho_{\text{cond}}g}{3\rho}} \quad Re > 70, Kn < 1, \text{ and} \quad (5)$$

$$v_{\text{fall}}(r) = r \cdot \sqrt{\frac{\pi\mu}{2N_A k_b T}} \left(\frac{8\rho_{\text{cond}}g}{27\rho} \right) \quad Kn > 1. \quad (6)$$

In Equations 4, 5, and 6, N_A is Avogadro’s number ($6.022 \times 10^{23} \text{ mol}^{-1}$), k_b is Boltzmann’s constant ($1.38 \times 10^{-16} \text{ erg K}^{-1}$), and g is the local gravitational acceleration. The quantity ρ_{cond} represents the mass density of the particle itself, for which we use the bulk density of a solid or liquid phase having the composition of the condensate. The parameters used for each condensate we have treated—iron, forsterite, gehlenite, and water—are listed in Table 2. The mass density of the gas ρ depends on temperature and pressure through the equation of state. The terminal velocity of particles depends also on the local acceleration of gravity, g , which varies considerably among the SMO population (see Section 3). In the Stokes solution, Equation 4, the terminal velocity is proportional to the square of the radius of the falling sphere. In the turbulent regime, Equation 5, it is proportional to the square root of the radius. In the gas kinetic (or large Knudsen number) regime, Equation 6, the terminal velocity increases linearly with particle radius. The gravitational fallout timescale is inversely proportional to the terminal velocity: $\tau_{\text{fall}} = H/v_{\text{fall}}$, where $H = \frac{RT}{\mu g}$ is the atmospheric scale height. We describe in Section 2.3 our procedure for differentiating between the Reynolds number regimes, which is necessary to calculate τ_{fall} and the other microphysical timescales.

The τ_{conv} timescale represents the convective upwelling of particles. Although convective upwelling is not itself a particle growth process, convective updrafts hold small cloud particles aloft in the atmosphere so that they accumulate more material via coagulation, coalescence, etc. We define the timescale characterizing convective updrafts as

$\tau_{\text{conv}} = H/v_{\text{conv}}$. The convective timescale is thus the time required for gas parcels to rise through a pressure scale height. The upward convective velocity, v_{conv} , is estimated via a mixing length prescription in the atmosphere code.

The nucleation timescale, τ_{nuc} , characterizes particle growth via homogeneous nucleation, in which highly supersaturated vapor condenses spontaneously due to rapid collisions between the vapor molecules. For the nucleation timescale, we employ the classical homogeneous nucleation theory, in which droplets form in free space as a result of chance collisions between the molecules of the supersaturated vapor. This process is rarely observed to occur in nature because its timescale will be longer in almost all cases than τ_{cond} , which characterizes the condensation growth of a population of particles via heterogeneous nucleation. Condensation growth means the conversion of vapor to particles, whether they be in the liquid or solid phase. For example, the phase diagram of iron indicates that iron will condense into liquid particles above 1800 K. However, we ignore the distinction between liquid and solid particles because the particles are small enough that the flattening effect during free-fall is negligible. In heterogeneous nucleation, particles nucleate onto seed particles, called condensation nuclei, which are presumed to populate the region of condensation. As discussed, when heterogeneous nucleation is efficient, condensation may begin even when the level of supersaturation is quite low ($< 1\%$). Neither nucleation process represented by τ_{nuc} and τ_{cond} apply to the species that appear due to chemical reactions (e.g., forsterite and gehlenite) rather than from a supersaturated vapor. The nucleation timescale expressions apply only to the species (e.g., iron and water) for which the condensate forms directly from a vapor of the same composition.

For the condensation timescale, τ_{cond} , we consider nucleation onto seed aerosols, also known as condensation nuclei. The assumption of a low maximum supersaturation of the condensable vapor— $\mathcal{S}_{\text{max}} = 1\%$ throughout (see Section 2.1)—is equivalent to the assumption that condensation nuclei are abundant in the upper atmosphere; i.e., these are “dirty” atmospheres. We have not attempted in the present model to calculate the compositions or exact abundances of these condensa-

tion nuclei. Our assumed value for \mathcal{S}_{max} is based rather on the recognition that the complex chemistry occurring in SMO atmospheres will likely generate a plethora of molecules suitable as seeds for the onset of heterogeneous nucleation. The expressions for the condensation timescale, which depend on the Knudsen number regime, are adapted from Rossow (1978):

$$\tau_{\text{cond}} = \rho r^2 \left(\frac{\rho_{\text{cond}} RT}{4\eta\mu P_{\text{sat}} \mathcal{S}_{\text{max}}} \right), \quad \text{Kn} < 1, \quad (7)$$

$$\tau_{\text{cond}} = r \left(\frac{\rho_{\text{cond}} RT}{3P_{\text{sat}} \mathcal{S}_{\text{max}}} \right) \left(\frac{\pi}{2\mu N_A k_b T} \right)^{1/2}, \quad \text{Kn} > 1. \quad (8)$$

In Equations 7 and 8, P_{sat} is the saturation vapor pressure defined in Equation 1, and ρ_{cond} is the mass density of the condensate. The other variables are the same as in Equations 4, 5, and 6. The mass densities of the four condensates treated in this paper are given in Table 1.

The condensation timescale given in Equations 7 and 8 assumes that heterogeneous nucleation dominates over homogeneous nucleation; i.e. $\mathcal{S}_{\text{max}} \ll 1$. We relax this assumption by incorporating the process of homogeneous nucleation explicitly (τ_{nuc}). It should be noted, however, that the inclusion of τ_{nuc} will only be important if the maximum supersaturation parameter is assumed to be large ($\mathcal{S}_{\text{max}} \gg 1$). We present homogeneous nucleation as a feature of the cloud model so that particle growth can be treated in the extreme case of very high supersaturations. As we have indicated, however, this situation is not likely in brown dwarf atmospheres. In most cases, homogeneous nucleation will be orders of magnitude slower than condensation growth by heterogeneous nucleation (i.e., $\tau_{\text{nuc}}^{-1} \ll \tau_{\text{cond}}^{-1}$).

For the timescale of homogeneous nucleation, we have adapted expressions from Stevenson & Lunine (1988) for large Knudsen numbers:

$$\tau_{\text{nuc}} = \frac{\rho_{\text{cond}} r L^2 \mu}{c_{\text{sound}} RTP [\exp(2\epsilon_{\text{surf}}\mu/RT\rho_{\text{cond}}r) - 1]} \quad (\text{Kn} > 1). \quad (9)$$

Here, r is the particle radius, L is the latent heat of vaporization, ϵ_{surf} is the surface tension of the condensed liquid molecules, $c_{\text{sound}} = \sqrt{RT/\mu}$ is the sound speed in the atmosphere, and P and T are the ambient temperature and pressure. We list the values of these parameters for iron and water

in Table 2. This expression is derived from Equations 3-5 of Stevenson & Lunine (1988) by taking $\tau_{\text{nuc}} = r \left[\frac{dr}{dt} \right]^{-1}$ and then substituting in from the ideal gas equation of state and the Clausius-Clapeyron equation to eliminate the particle number density, saturation vapor pressure, and the vapor pressure temperature gradient. We take the efficiency of heat exchange in Equation 3 of Stevenson & Lunine (1988) to be 100% and the average relative velocity of cloud particles colliding with the local hydrogen to be c_{sound} .

The τ_{nuc} expression for large Knudsen numbers represents the timescale for the growth of an embryonic cloud particle that must release the latent heat of condensation through collisions with the surrounding hydrogen (Stevenson & Lunine 1988). It is possible, however, for particles in high-temperature environments to grow by releasing the latent heat of condensation simply through radiatively cooling. We therefore include in the model an estimate of the radiative cooling timescale, which is compared with Equation 9 in the calculation. If $\tau_{\text{rad}}^{-1} > \tau_{\text{nuc}}^{-1}$, and the mean free path of particles is greater than the particle size, we use τ_{rad} in place of τ_{nuc} . The equation we use to approximate τ_{rad} is adapted from Woitke (1999):

$$\tau_{\text{rad}} \approx (2 \times 10^{-2} \text{ sec}) \cdot \left(\frac{\rho_{\text{cond}}}{1 \text{ g cm}^{-3}} \right) \times \left(\frac{\mu_p}{1 \text{ g mol}^{-1}} \right)^{-1} \left(\frac{T}{1000 \text{ K}} \right)^{-4}. \quad (10)$$

In Equation 10, μ_p is the molecular weight of the condensate (as distinct from $\mu \approx 2.36 \text{ g mol}^{-1}$, the mean molecular weight of the atmospheric gas mixture). The values of μ_p for the four condensates treated herein are given in Table 2.

It should be noted that in a very high temperature, low density environment, in which the release of latent heat is extremely fast, the limiting timescale for homogeneous nucleation will be neither τ_{nuc} nor τ_{rad} but the timescale for the diffusion of vapor molecules to the surface of the grain. We do not calculate this timescale in the present model. For the purposes of SMO atmospheres, however, this regime will never be realized in practice because the condensation temperatures of even the most refractory compounds rarely exceed 2000 K. Therefore, although the limit of $\tau_{\text{rad}} \rightarrow 0$ in this formulation appears to be potentially prob-

lematic, the temperature constraints ensure that τ_{rad} cannot be arbitrarily small. Hence, for use in the calculation of SMO clouds, it is reasonable to assume that the shorter of the two timescales, τ_{nuc} and τ_{rad} , determines the particle's homogeneous nucleation rate.

The constant preceding Equation 10 is strictly correct only for highly opaque species having high extinction efficiencies. This is appropriate for the condensates we focus on here, although the timescale for radiative cooling will be longer by a factor of ten or a hundred than the timescale shown in Equation 10 if the particles are mostly transparent. In cases in which the τ_{rad} timescale dominates the particle sizes, a more accurate approximation than we have made in Equation 10 should be calculated by integrating the extinction efficiency over wavelength; e.g., see Equation 17 of Woitke (1999).

The more common case of small Knudsen numbers, which corresponds to high atmospheric gas density, is a commonly used meteorological expression; see Rogers & Yau (1989). The low Knudsen number expression for τ_{nuc} is written in terms of the critical radius at which the equilibrium vapor pressure over the surface of a particle equals the ambient vapor pressure. The equilibrium vapor pressure over the surface of a liquid particle, because of its finite curvature, is in general higher than the equilibrium vapor pressure over a flat surface of the liquid, which is the saturation vapor pressure normally measured in the laboratory. Therefore, the critical radius of the liquid particle will only be attained when the saturation ratio exceeds unity; i.e., when the actual ambient pressure exceeds the saturation vapor pressure. The critical radius therefore depends on the supersaturation \mathcal{S}_{max} (Rogers & Yau 1989):

$$r_c = \frac{2\mu_p \epsilon_{\text{surf}}}{\rho_{\text{cond}} RT \ln(1 + \mathcal{S}_{\text{max}})}. \quad (11)$$

Unlike the gas kinetic regime, in which the removal of latent heat limits the rate at which particles can grow by nucleation, in the classical gas regime, the nucleation rate of particles is determined by the rate at which supercritical droplets are formed; i.e., droplets larger than the critical radius above which particles grow spontaneously. The expression for τ_{nuc} in terms of the critical droplet radius r_c , adapted from Rogers & Yau

(1989), reads

$$\tau_{\text{nuc}} = \frac{1}{\bar{P}} \sqrt{\frac{\mu_{\text{p}} k_{\text{b}} T}{8\pi N_{\text{A}} r_{\text{c}}^4}} Z^{-1} \exp\left(\frac{4\pi r_{\text{c}}^2 \epsilon_{\text{surf}}}{3k_{\text{b}} T}\right) \quad (\text{Kn} < 1). \quad (12)$$

In Equation 12, Z is the dimensionless Zeldovich or non-equilibrium factor, which depends on temperature and the physical properties of the condensate. The equation for Z , given by Jacobson (1999), is

$$Z = \frac{\mu_{\text{p}}}{2\pi r_{\text{c}}^2 \rho_{\text{cond}} N_{\text{A}}} \sqrt{\frac{\epsilon_{\text{surf}}}{k_{\text{b}} T}}. \quad (13)$$

The Zeldovich factor accounts for the differences between equilibrium and non-equilibrium cluster concentrations in the classical homogeneous nucleation theory used to derive Equations 11 and 12.

Coagulation and coalescence represent particle growth due to collisions. The coagulation timescale, τ_{coag} , refers to the formation of larger particles by the collision of smaller particles. It therefore depends primarily on the thermal temperature, viscosity, and the number density of cloud particles. The coalescence timescale, τ_{coal} , characterizes the growth of particles by coalescence, in which large particles having high downward velocities in the fluid overtake and merge with small, slowly falling particles. Thus, coalescence refers to the collisional process caused by the different fall speeds of different sized particles, whereas coagulation is collisional growth resulting from Brownian motion. Both processes proceed at a rate proportional to the particle number density, N , since the total amount of material available for condensation is conserved. The number density of cloud particles is given in terms of the gas density as

$$N = q_{\text{c}} \left(\frac{\rho}{\mu}\right) \left(\frac{3\mu_{\text{p}}}{4\pi\rho_{\text{cond}}r^3}\right). \quad (14)$$

In Equation 14, r is the cloud particle radius, ρ is the mass density of the surrounding gas (as given by the equation of state), ρ_{cond} is the mass density of the condensate, and q_{c} is the condensate mixing ratio by number, which depends on the specific rainout prescription applied. The rainout scheme we employ to compute the variation of q_{c} with height above the cloud base is explained in Section 2.3.

Given the particle number density, N , the timescale for coagulation in terms of the radius

of the condensed particle, r , is given by

$$\tau_{\text{coag}} \equiv \frac{N}{dN/dt} = \frac{3\eta}{4k_{\text{b}} T \epsilon_{\text{coag}}} \frac{1}{N}, \quad \text{Kn} < 1 \quad (15)$$

$$\tau_{\text{coag}} = \frac{1}{4\epsilon_{\text{coag}}} \sqrt{\frac{\rho_{\text{cond}}}{3rk_{\text{b}} T}} \frac{1}{N}, \quad \text{Kn} > 1. \quad (16)$$

Here, ϵ_{coag} is the coagulation efficiency, which is a free parameter of the model. We discuss this further in Section 2.4.

Our final microphysical timescale, τ_{coal} , characterizes the process of coalescence, in which larger particles overtake and coalesce with smaller particles. For coalescence, the Reynolds number again plays an important role because—unlike coagulation—coalescence pertains specifically to the merging of particles of greatly different radii whose interaction depends on the nature of the surrounding flow fields. The coalescence expressions are adapted from Rossow (1978), although we have introduced an extra free parameter into the equations, the efficiency for coalescence, ϵ_{coal} :

$$\tau_{\text{coal}} = \frac{1}{r^4 \epsilon_{\text{coal}}} \left(\frac{9\eta}{\pi\rho_{\text{cond}}g}\right) \frac{1}{N}, \quad \text{Re} < 70, \text{Kn} < 1 \quad (17)$$

$$\tau_{\text{coal}} = \frac{1}{\epsilon_{\text{coal}}} \sqrt{\frac{3\rho}{10\pi^2\rho_{\text{cond}}r^5g}} \frac{1}{N}, \quad \text{Re} > 70, \text{Kn} < 1 \quad (18)$$

$$\tau_{\text{coal}} = \frac{1}{r^3 \epsilon_{\text{coal}}} \left(\frac{27\rho}{4\pi\rho_{\text{cond}}g}\right) \sqrt{\frac{2RT}{\pi\mu}} \frac{1}{N}, \quad \text{Kn} > 1. \quad (19)$$

As we discuss in Section 2.4, coalescence is important only for liquid particles. This is the only case in our model in which the distinction between liquid and solid particle formation is important. Thus, for iron cloud formation above 1800 K, coalescence will potentially be important, and it can be important for water clouds, but we ignore it for the silicate clouds.

2.3. Our Cloud Code

The code proceeds in two stages: (1) determination of the cloud base globally in the atmosphere, and then (2) particle growth at each atmospheric temperature–pressure level. The algorithm is run for each of the atmospheric temperature–pressure profiles, which differ in effective temperature and gravity, and for each condensable species separately. In our model, we ignore *core–mantle* grains

composed of molecules of two or more of the major species. These types of condensates could potentially be important in regions in which several major constituents in the equilibrium vapor mixture form at similar temperatures and pressures. In the present cloud model, we do not treat the growth of grains composed of multiple chemical phases.

We list in Table 2 the input parameters for the four condensable species treated herein.

In stage (1), two cases must be treated separately, as explained above. In the case of homogeneous condensation, we calculate the intersection between the partial pressure of the condensable vapor and its saturation vapor pressure curve and identify the condensation level using Equation 1. In the case of heterogeneous condensation, in which the condensing chemical is not present in vapor form below the cloud base, we determine the cloud base by using the chemical equilibrium model of Burrows & Sharp (1999) (see Figure 1).

In stage (2), we calculate the modal size of particles, which are assumed to be spherical, at each atmospheric temperature–pressure level. The model outputs the modal particle radius. This radius is determined by growing embryonic particles of radius $\sim 10 \text{ \AA}$ slowly until the various competing particle growth timescales are balanced by the timescale of gravitational fallout. For the most probable particle radius, the sedimentation timescale equals the shortest of the growth timescales:

$$\tau_{\text{fall}} = \text{Min} \{ \tau_{\text{nuc}}, \tau_{\text{cond}}, \tau_{\text{coag}}, \tau_{\text{coal}}, \tau_{\text{conv}} \}. \quad (20)$$

Note that for homogeneously condensing species in the gas kinetic regime ($\text{Kn} > 1$), it may be that radiative cooling, rather than the release of latent heat by collisions with atmospheric hydrogen, is the dominant process limiting the rate of particle growth. Therefore, if the Knudsen number is greater than one and $\tau_{\text{rad}}^{-1} > \tau_{\text{nuc}}^{-1}$, we replace τ_{nuc} in Equation 20 with the timescale for particles to release the latent heat of condensation by radiation, τ_{rad} . Additionally, as we have stated in Section 2.2, nucleation does not apply to the case of chemical clouds (Rossow 1978), and coalescence is inefficient between solid particles. The condensed particles can only accumulate more material by coagulating under the influence of convective updrafts. Hence, for forsterite and gehlenite, the fall timescale must balance the minimum of the two

timescales relevant for heterogeneously condensing clouds: τ_{coag} and τ_{conv} .

The timescales in Equation 20 depend on the Knudsen and Reynolds numbers (see Section 2.2). We therefore need a prescription to determine which physical regime applies as the particles are grown. Because the Reynolds number depends on velocity, and the velocity depends on the Reynolds number, calculating the two quantities independently for a given particle size and atmospheric parameters is a circular problem. There are no difficulties if the Knudsen number is larger than one, since the gas kinetic terminal velocity in that case does not depend on the Reynolds number; the velocity to use in this case is given by Equation 6. To differentiate between Reynolds number regimes in the small Knudsen number case (i.e., Equations 4 and 5), we use the following procedure based on the fact that each of the two expressions for v_{fall} can be calculated independently of the Reynolds number.

At each point in the particle growth phase, we use *both* Equations 4 and 5, along with the known atmospheric parameters and the current particle size. In solving for the terminal velocity, we substitute the SMO surface gravity, g_{surf} , in for g , the local gravitation acceleration. We then calculate two temporary values for the Reynolds numbers, one for each of the velocities calculated. If these two independently computed Reynolds numbers are both smaller than our Reynolds number cutoff point of 70 between laminar and turbulent flow (Rossow 1978), we take the flow around the particles to be laminar and adopt the Stokes terminal velocity, Equation 4, as the actual terminal velocity. Likewise, if they are both larger than the cutoff, we take the flow around the particles to be turbulent and adopt the turbulent terminal velocity, Equation 5, as the actual terminal velocity.

The intermediate case, in which one temporary Reynolds number is larger than the cutoff but the other is smaller than the cutoff, is more difficult to resolve. We settled on the choice of using the lesser of the two terminal velocities as the actual terminal velocity. Although this could have been handled in a variety of ways, the inherent ambiguities could not have been eliminated without detailed knowledge of the drag coefficient, which unfortunately depends in general on the Reynolds number. Ours was the most conservative choice

TABLE 2
CONDENSATE PHYSICAL PROPERTIES

Model Parameter	Iron	Forsterite	Gehlenite	Water
Molecular weight, μ_p [g mol ⁻¹]	55.8	140.7	274.2	18.0
Mass Density, ρ_{cond} [g cm ⁻³]	7.9 ^a	3.2	3.0	1.0 ^a
Mole Fraction, q_{below} ^b	5.4×10^{-5}	3.2×10^{-5}	1.8×10^{-6}	1.4×10^{-3}
Surface Tension, ϵ_{surf} [ergs cm ⁻²]	200	75
Latent Heat of Vaporization, L [ergs g ⁻¹]	6.34×10^{10}	4.87×10^{12}

^aWe are ignoring here the minor differences between the densities of the liquid and solid phases of iron and water (Lide 1991, CRC Handbook).

^bThe q_{below} parameter is the mole fraction of condensable vapor just below the cloud base; the calculation of q_{below} assumes a solar abundance distribution of the elements (Anders & Grevesse 1989).

NOTE.—Values for the surface tension and latent heat of vaporization are taken from Lide (1991, CRC Handbook). They are used to derive τ_{nuc} using the classical homogeneous nucleation theory and are therefore not applicable to the heterogeneously condensing species (see Section 2.2). Note also that the mole fractions listed apply only to the cloud base (i.e., the condensation level, as shown in Figure 1). Above the cloud base, the mole fraction of total condensable material in the cloud drops off much more steeply than the gas pressure (as prescribed in Equations 21 and 22).

for a first-order estimate of the terminal velocity. With this procedure in place to calculate the terminal velocity of particles, the effective Reynolds number—which is used to calculate all the other timescales—is computed directly from its definition in Equation 3, with v_{fall} substituted in for the relative velocity, v .

Equation 20 shows the role of convection in this model. Convection directly opposes gravitational sedimentation. In the presence of sufficiently vigorous convection, therefore, the particles may continue to accumulate material until their terminal velocities become equal to the convective updraft velocity.

The simple cloud model delineated above is a first-order estimate of SMO particle sizes. The true particle sizes could very well deviate from the values computed by a factor of order unity, though we believe that this factor will be the same for all objects studied because the systematic errors depend on our assumptions of the unknown parameters of the model, assumptions which we have applied consistently throughout the computations.

Our treatment of rainout, in which condensates settle gravitationally and thus become depleted from the upper atmosphere, differs between homogeneously and heterogeneously condensing species. Depletion of the condensate with height must differ between these two different types of clouds because homogeneous condensation involves a pressure equilibrium between the vapor and the condensed phase (See Section 2.2), whereas heterogeneous condensation produces the condensate directly through exothermic chemical reactions.

For the purposes of this discussion, we adopt the notation of Ackerman & Marley (2001) for the relevant mixing ratios: q_v = moles of vapor per mole of atmosphere, q_c = moles of condensate per mole of atmosphere. The total mixing ratio is $q_t = q_v + q_c$. We also define q_{below} as the mixing ratio by number (or mole fraction) of condensable vapor just below the cloud base, which equals q_t at that level, since $q_c = 0$ by definition below the cloud base (i.e., at levels in the atmosphere where Equation 1 is not satisfied). The values of q_{below} for each condensable treated herein are given in Table 2.

For both homogeneously and heterogeneously condensing species, we assume aggressive rainout

such that the total material available to condense into particles drops off with pressure much more steeply than the gas pressure. That is, at the condensation level, the mixing ratio by number (or equivalently, the mole fraction) of the condensing species is taken to be equal to the maximum partial pressure attained by that species in a gas of solar composition (i.e., parameter q_{below} in Table 2). For heterogeneously condensing species, q_{below} is constrained by the maximum partial pressure of the least abundant of the constituent molecules combining to form the condensate. For example, in the case of forsterite, the magnesium abundance in the gas controls the value of q_{below} . We have assumed a solar abundance of magnesium in the atmosphere below the forsterite condensation level. High above the condensation level, however, the mixing ratio of cloud-forming material is significantly reduced from the equilibrium ratio, and the cloud becomes more and more tenuous with decreasing pressure.

For homogeneously condensing species, our rainout prescription is based on the assumption that all of the supersaturated vapor above the base of the cloud will condense. As we have discussed in Section 2.1, the onset of particle formation requires a supersaturated environment, which thus elevates the cloud base above the level where precise saturation of condensable vapor is attained. Once present, however, particles remain thermodynamically stable unless the saturation ratio drops to below one, which will not happen without a temperature inversion in the atmosphere’s thermal profile. For already existent particles or cloud particle embryos, the vapor in equilibrium with the particles remains exactly at saturation. All excess material goes into the condensate. Hence, throughout the cloud, we take $q_v = P_{\text{sat}}/P$, where P_{sat} is the saturation vapor pressure and P is the gas pressure. Notice that this ratio decreases with altitude because P_{sat} decreases with pressure much more steeply than the gas pressure, P . It therefore follows that the partial pressure of the condensable vapor required to maintain a saturated environment will be extremely small high above the condensation level. Though the mole fraction of condensing vapor, q_v , is constrained by the requirement that the condensed phase remain thermodynamically stable during particle growth, we still need the total

number mixing ratio (i.e., mole fraction) of condensable material, q_t , in order to determine q_c , the condensate number mixing ratio.

The character of the rainout itself derives from the assumption that the total material available for condensation above the cloud base follows the saturation vapor pressure and *not* the gas pressure. We use $q_t = (1 + \mathcal{S}_{\max}) P_{\text{sat}}/P$, which implies that the total condensable material is constrained to drop off with altitude proportionally to the saturation vapor pressure. This is an assumption of the cloud model. It is not based on a rigorous derivation of the total mixing ratio with altitude. The justification for the rainout scheme is that once condensation begins in the atmosphere, with subsequent growth and gravitational settling of particles, the condensable material can no longer remain well-mixed in the atmosphere, as we assume it had been below the cloud base. Therefore, the total number of moles of condensable material per mole of gas will decrease rapidly from its initial value with increasing height above the condensation level. By contrast with our rainout scheme, a no-rainout model would be one in which the fraction of condensed material follows the gas pressure; i.e., q_t equals a constant throughout the cloud. In this case, the ratio of condensate to condensable vapor, q_c/q_v , will increase with height above the base of the cloud.

With the above considerations, it is straightforward to calculate q_c as simply the difference between the total number mixing ratio of condensable material and the number mixing ratio of condensable vapor: $q_c = q_t - P_{\text{sat}}/P$. We therefore obtain the following equation for q_c :

$$q_c = \mathcal{S}_{\max} \cdot \frac{P_{\text{sat}}}{P} = \mathcal{S}_{\max} \cdot q_{\text{below}} \cdot \frac{P_{c,1}}{P}. \quad (21)$$

In Equation 21, $P_{c,1}$ denotes the saturation vapor pressure curve—given by P_{sat} , as in Equation 1—adjusted to resemble a condensation curve by applying the mixing ratio in a solar composition gas; i.e., $P_{\text{sat}} = q_{\text{below}} \cdot P_{c,1}$. For example, the dotted curve labeled “Fe” in Figure 1 shows the $P_{c,1}$ for iron, *not* the iron saturation vapor pressure curve. The subscript notation for $P_{c,1}$ simply refers to the “effective” iron condensation curve as derived from the saturation vapor pressure curve. The rainout is expressed in terms of $P_{c,1}$ for comparison with the analogous prescription for rain-

out in a heterogeneous cloud (Equation 22). The quantity P in Equation 21 is the total gas pressure in the atmosphere. As is clear from comparing the thick dotted Fe line in Figure 1 with one of the gas pressure profiles, P decreases with height above the cloud base much less steeply than $P_{c,1}$. The assumption of a constant supersaturation throughout the cloud, which we have made in fixing the value of \mathcal{S}_{\max} , leads to a cloud with a very low ratio of condensed material to total condensable material unless $\mathcal{S}_{\max} \gg 0.01$.

For heterogeneously condensing clouds, we refer to the condensation curves (denoted $P_{c,1}$ in Equations 21 and 22) of forsterite and gehlenite as shown in Figure 1. We make the assumption for a heterogeneously condensing cloud that the total mixing ratio, q_t , follows the condensation curve above the cloud base. This assumption is analogous to the assumption used to derive Equation 21 for homogeneously condensing clouds that the total mixing ratio follows the saturation vapor pressure curve. However, in a heterogeneous (or chemical) cloud, once the condensate appears in chemical equilibrium, we argue that the solid phase will then be strongly favored, and hence the product chemical will be fully condensed. Thus, for heterogeneous condensates, $q_v = 0$ and $q_c = q_t$. The rainout formula for heterogeneous species is therefore quite similar to Equation 21, without the reduction of q_c relative to q_t by the supersaturation factor, which is not relevant for chemical clouds:

$$q_c = q_{\text{below}} \cdot \frac{P_{c,1}}{P}. \quad (22)$$

In Equation 22, the quantity $P_{c,1}$ represents the chemical equilibrium condensation curve of the condensing species, as shown for forsterite and gehlenite in Figure 1. It is apparent from Figure 1 that this rainout prescription sequesters most of the condensate within a scale height of the cloud base, since the condensation pressure drops off so steeply relative to the gas pressure. For example, consider the forsterite cloud shown in Figure 1 for the brown dwarf model at $T_{\text{eff}} = 900$ K and $g_{\text{surf}} = 3 \times 10^5 \text{ cm s}^{-2}$. At the forsterite cloud base, which is at about $T \approx 2000$ K and $P \approx 125$ bars, the mixing ratio of forsterite is just determined by the abundance of magnesium in the mixture, or $q_c = q_{\text{below}} = 3.2 \times 10^{-5}$. Higher up in the atmosphere (in altitude), at $T \approx 1700$ K and

$P \approx 70$ bars, Equation 22 shows that q_c , which follows the condensation curve, is reduced by a factor ~ 100 from its value at the cloud base. However, the gas pressure is down by only about 55%, or $\sim \frac{1}{2}$ a scale height.

Equations 21 and 22 show that, in the present model, virtually all of the atoms in the solar-composition gas that are initially available for condensation become sequestered in the condensate within a scale height of the atmosphere. For example, because the limiting atomic species for the formation of forsterite is magnesium, and forsterite is favored chemically below about 2000 K, magnesium will have rained out near the forsterite cloud level, and no magnesium will be available for further condensation into other chemicals high above the forsterite cloud level. Rainout thus depletes the atmosphere of the most refractory elements at progressively lower temperatures and pressures.

Each timescale characterizes the average (or characteristic) effectiveness of each of the competing microphysical processes in the system. Our computed particle sizes thus represent the most probable particle size in the distribution of particle sizes appearing at each pressure level. To the order of the accuracy of the particle sizes themselves, therefore, the resulting particle sizes in each pressure level will equal the mode of the particle size distribution.

We make no attempt in the present model to calculate the particle size distribution for each cloud layer. Rather, for the purposes of calculating the opacity of clouds and using these opacities in SMO spectral models, we assume a functional form for the particle size distribution that is consistent with measurements of particle size distributions attained in Earth’s water clouds (Deirmendjian 1964). We use the form of the Deirmendjian (1964) exponentially decaying power law employed by Sudarsky et al. (2000):

$$n(r) \propto \left(\frac{r}{r_0}\right)^6 \exp\left[-6\left(\frac{r}{r_0}\right)\right], \quad (23)$$

where $n(r)dr$ is the number of particles per cubic centimeter having radii $r \rightarrow r + dr$. We employ the cloud model described above to determine the mode of the distribution, r_0 .

2.4. Free Parameters

In addition to S_{\max} , the assumed maximum supersaturation, the free parameters of the cloud model include the elemental abundances and the sticking coefficients for coagulation and coalescence. The vapor mixing ratios have been calculated assuming solar (Anders & Grevesse 1989) abundances of the elements in the atmosphere.

Coagulation and coalescence are not expected to be 100% efficient in all cases because some molecules stick together when they collide more easily than others. Therefore, we have divided the timescales for coagulation and coalescence, given in Rossow (1978) as τ_{coag} and τ_{coal} , by efficiency parameters ϵ_{coag} and ϵ_{coal} .

Coalescence between solid particles is extremely inefficient (Rossow 1978). Coalescence will therefore not be important for forsterite and gehlenite because the solid phase is strongly favored once the temperature decreases sufficiently for the chemical to appear (see Figure 1). Therefore, for the heterogeneously condensing materials, we have ignored coalescence ($\epsilon_{\text{coal}} = 0$). For the species condensing into liquid particles (iron and water), we have taken $\epsilon_{\text{coag}} = 10^{-1}$ and $\epsilon_{\text{coal}} = 10^{-3}$ (Lunine et al. 1989). We have also used $\epsilon_{\text{coag}} = 10^{-1}$ for the coagulation efficiency of heterogeneously condensing species. Subsequently, we will argue that this choice is relatively unimportant because coagulation and coalescence generally operate more slowly, for the atmospheres we are considering here, than heterogeneous nucleation and convection. We discuss in Section 3.4 how varying these parameters affects the general features of the cloud.

3. Model Results

3.1. Modal Particle Sizes

We compute particle sizes for each of four species on a set of atmospheric models spanning the ranges $T_{\text{eff}} = 600 - 1600$ K and $g_{\text{surf}} = 1.78 \times 10^3 - 3 \times 10^5$ cm s⁻². We chose the most abundant condensable species in the solar-composition mixture: iron, forsterite, and water. Iron and forsterite are the most abundant high-temperature condensates (Lunine et al. 1989). Although we have included one of the calcium-aluminum silicates, gehlenite, and these refractory

species do condense into clouds, their abundance in a solar-composition gas is lower than that of iron or forsterite by a factor of about ten (Lunine et al. 1989). Thus, the contribution of the calcium and aluminum silicates to the total opacity is expected to be relatively minor. Nevertheless, the condensation of the calcium and aluminum silicates is important for sequestering calcium and aluminum at depth beneath the photospheres of cooler SMOs. Moreover, the most refractory calcium and aluminum silicates can potentially serve as nucleation sites for the condensation of iron vapor via heterogeneous nucleation at low supersaturations.

3.2. Trends With Brown Dwarf Gravity and Effective Temperature

Figures 2, 3, and 4 show the particle sizes computed by our model for a range of brown dwarf atmospheric profiles. Each circled point represents, for the atmospheric profile to which it applies, the grain size computed by our model at the initial cloud level (i.e., the cloud base). As we discuss further in Section 3.3, these are in general the largest modal particle sizes for the cloud, since particle sizes decrease with height above the cloud base. The model atmosphere corresponding to each circled point is indicated by its position on the diagram: gravity increases from left to right, whereas effective temperature increases from bottom to top in the field. These graphs say nothing about the distribution of material above the cloud base. They apply only to the initial condensation level where the mass density of material is greatest. Figure 2 shows the results for iron grains, which condense directly from iron vapor. Figure 3 shows the analogous results for forsterite grains, which appear as a result of chemistry (i.e., heterogeneous condensation). Figure 4 shows the same for gehlenite, which also condenses heterogeneously.

Figures 2, 3, and 4 show that cloud grains in hot brown dwarfs, for a fixed surface gravity, are systematically larger than in cold brown dwarfs. Similarly, cloud particles in objects with high surface gravities, for a fixed effective temperature (e.g., older brown dwarfs), are systematically smaller than in objects having low surface gravities.

The trend with surface gravity is simple to explain: particles settle more quickly in high-gravity

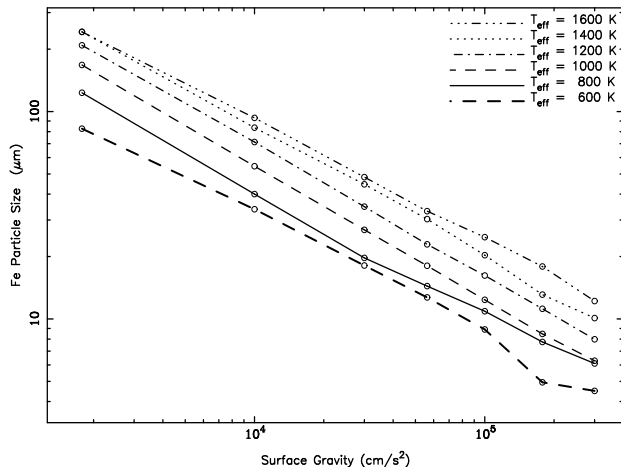


Fig. 2.— The grain sizes of iron (Fe) at the cloud base for a range of brown dwarf atmospheric temperature–pressure profiles. The figure displays the modal particle sizes obtained by applying the model described in Section 2 to each model brown dwarf atmosphere. The profiles span a range of effective temperatures and surface gravities from $T_{\text{eff}} = 600 - 1600$ K and $g_{\text{surf}} = 1.78 \times 10^3 - 3 \times 10^5$ cm s^{-2} . Each circled point corresponds to a different brown dwarf model atmosphere whose effective temperature and gravity depend on the point’s location in the field. The figure shows that high-gravity brown dwarfs will have characteristically smaller particle sizes than low-gravity brown dwarfs for a given effective temperature. Similarly, hotter brown dwarfs will exhibit larger particle sizes, for a given surface gravity, than cooler brown dwarfs.

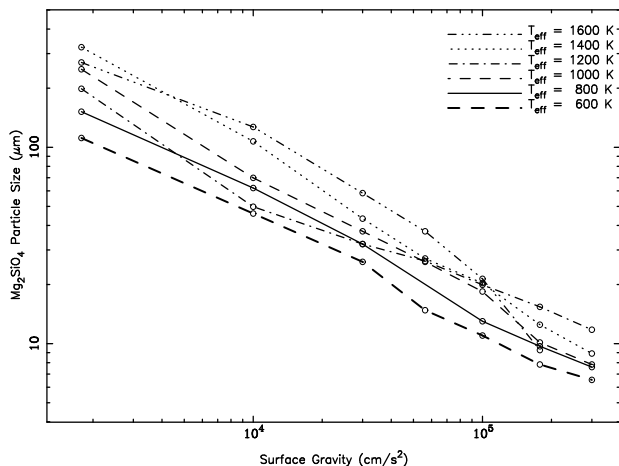


Fig. 3.— Companion to Figure 2: shows similar trends for forsterite (Mg_2SiO_4) particle radii. The forsterite particles become extremely large ($\sim 350 \mu\text{m}$) in very low gravity objects. Because forsterite forms in abundance in the atmosphere, the optical effects of forsterite clouds are potentially very important, depending on the particle sizes.

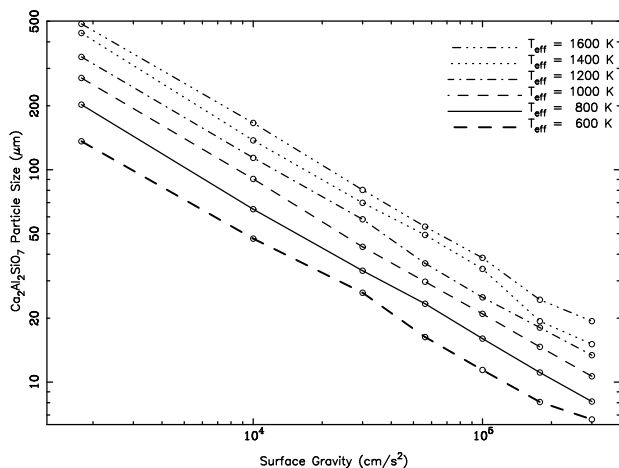


Fig. 4.— The particle size trends for the calcium–aluminum silicate gehlenite ($\text{Ca}_2\text{Al}_2\text{SiO}_7$). This species is less abundant than forsterite by about a factor of ten, but it has the important effect of sequestering Ca and Al in condensed form below the photosphere of the cooler objects.

environments. This appears to be the overriding effect governing particle size. Although both the atmospheric pressure and temperature at the cloud base are higher in high-gravity objects, and the convection therefore more rapid, gravity dominates and the resulting particles are smaller. For the lowest gravity objects, the forsterite particles grow quite large. They therefore contribute only negligibly to the total optical depth (Sudarsky et al. 2000).

The trend with effective temperature results from the difference in convective updraft velocity between colder and hotter objects. Objects with higher effective temperatures must transport a higher flux of thermal energy to the surface via interior turbulent convection. Therefore, the updrafts holding cloud particles aloft will be more rapid in the higher T_{eff} objects, resulting in larger particle sizes.

3.3. Cloud Decks in Convective vs. Radiative Regions

Brown dwarfs are almost fully convective, with only a thin radiative atmosphere (Basri 2000; Burrows et al. 2001). Convective uplifting sustains the particles against gravitational fallout. The effectiveness of this process depends on the velocity scale of the convection. Hence, the gradient in the convective velocity plays a role in determining particle size. Deep in the atmosphere, the brown dwarf is fully convective, with a relatively high updraft velocity (approaching $5 \times 10^3 \text{ cm/s}$). At higher altitudes, the updraft speed is small, but *not* zero. Therefore, clouds at depth are convective; clouds at altitude are quiescent. By quiescent, we mean clouds formed in convectively stable layers where the true lapse rate is shallower than the adiabatic lapse rate.

The updraft speeds observed in stably stratified layers in Earth’s atmosphere typically range from 1 – 10 cm/s. Clouds analogous to Earth’s stratus clouds are possible in quiescent layers of planetary atmospheres, even though the updraft speeds are smaller by a factor of a hundred or more than the typical speeds of convective updrafts (Rogers & Yau 1989). In the case of these stratiform clouds, small particle sizes (generally less than $10 \mu\text{m}$) lead to relatively slow sedimentation rates. Large-scale uplifting of a stable layer can thus replenish the cloud material lost by evap-

orating particles on a timescale of hours or days, which is rapid enough to sustain the cloud. Slow, large-scale updrafts, which we assume are occurring in these atmospheres, are too slow to affect the particles directly. Therefore, we do not include them as a growth process in the cloud model, as we have done for convective updrafts, but their existence is an important feature of the formation of quiescent clouds by maintaining the supersaturated environment necessary for particle growth.

Particles in quiescent clouds are generally smaller than particles in convective clouds. Figure 5 compares the particle sizes of condensed iron for a brown dwarf model having $T_{\text{eff}} = 1500$ K and $g_{\text{surf}} = 5.62 \times 10^4$ cm s $^{-2}$. The modal particle sizes in the cloud are shown for iron under two contrasting assumptions: (1) the cloud is convective (i.e., $\tau_{\text{conv}} = H/v_{\text{conv}}$), and (2) the cloud is radiative (i.e., $\tau_{\text{conv}} = \infty$). Our calculations suggest that for this atmosphere, a convective iron cloud is more realistic. We thus predict the solid curve for the actual particle size distribution in the cloud deck. Figure 5 compares the particle sizes obtained by activating and deactivating the convective uplifting mechanism.

Figure 5 shows, for this particular brown dwarf atmosphere, that cloud particles growing in a region of strong convective upwelling are largest near the cloud base but then diminish rapidly with height. This decrease in size is due to the proximity of the iron cloud base, for this particular model, to the radiative-convective boundary of the atmosphere, where the gradient in the upwelling velocity is steep. For convective clouds deep within the convective zone, where the upwelling velocity is nearly constant, the particle sizes will be more constant throughout the cloud deck. However, deep clouds will not strongly influence the object’s emergent spectrum.

If the cloud is radiative, the particles will not grow as large as they would under the influence of convection. Furthermore, their sizes will not decrease by more than a factor of two from base to cloud top. This result appears quite general for the radiative clouds we have investigated.

The structure of the cloud decks (e.g., as shown in Figure 5) of brown dwarfs is crucial for computing the optical depth of the cloud. For clouds in which the overall particle sizes decrease significantly with altitude above the cloud base, it

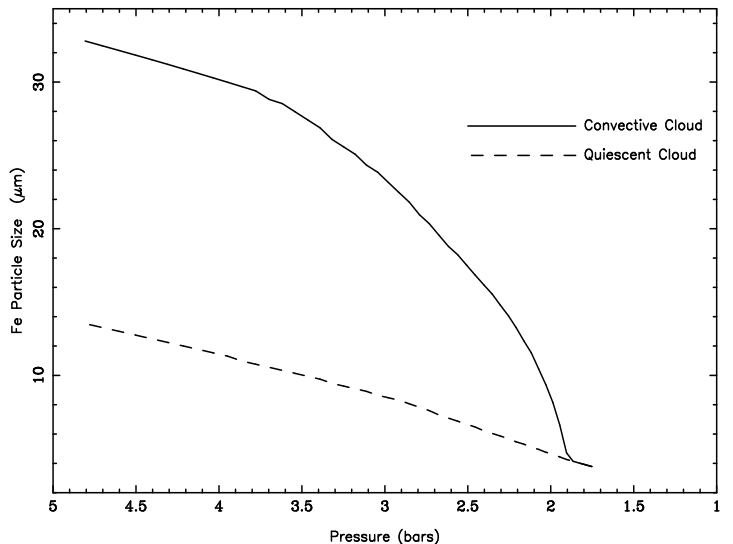


Fig. 5.— The structure of an iron cloud deck for a particular brown dwarf at $T_{\text{eff}} = 1500$ K and $g_{\text{surf}} = 5.62 \times 10^4$ cm s $^{-2}$, assuming a constant 1% maximum supersaturation during the entire particle growth phase. The dashed curve assumes that convection is not effective at sustaining particle growth. Therefore, the particles do not grow as large. For this radiative (or quiescent) cloud, the particle sizes vary by about a factor of two within an atmospheric scale height. On the other hand, for the convective cloud, in which we allow updrafts to sustain particle growth against gravitational sedimentation, the particles grow relatively large. Because the cloud base is slightly above the radiative-convective boundary of the profile, the updraft velocity decreases rapidly with height. Thus, for clouds forming near unity optical depth, we expect variable particle sizes from the cloud base to the cloud top. The cloud particle sizes for the convective cloud merges with the sizes obtained for the quiescent cloud once the updraft velocity becomes negligible. The exact cutoff for the cloud is somewhat arbitrary; we present a full scale height of both cloud decks. As we explain in our discussion of rainout in Section 2.3, the cloud is extremely thin this high above the cloud base, and the mole fraction of total condensing material, given by q_t , is depleted from its value at the cloud base, where $q_t = q_{\text{below}}$, by many orders of magnitude (see Equation 21).

may be that the bulk of the optical depth in the near-infrared will be contributed not by the lowest cloud layers but by intermediate layers having significant abundances of smaller particles.

3.4. Varying the Free Parameters

Among the model free parameters discussed above, the level of maximum supersaturation is the most problematic. The value of \mathcal{S}_{\max} is particularly difficult to calculate independently, and because the condensation timescale depends on it, \mathcal{S}_{\max} has a significant effect on the resulting particle size. This effect will be manifest in quiescent clouds but will be less important in convective clouds. This is because in rapidly convecting regions, convective upwelling can directly sustain particle growth.

Figure 6 shows, for one brown dwarf model, the effect of varying \mathcal{S}_{\max} on the modal particle size of a water cloud. For low levels of supersaturation, the particles grow to a radius of $\sim 50 \mu\text{m}$. In this case, abundant condensation nuclei raise the rate of heterogeneous nucleation high above the rate of homogeneous nucleation, and condensation can begin as soon as the atmosphere becomes slightly supersaturated. For high levels of supersaturation ($>10\%$), they grow much larger, to $\sim 150 \mu\text{m}$. In this clean atmosphere case, heterogeneous nucleation does not occur, and the partial pressure of water in the atmosphere must greatly exceed the saturation vapor pressure in order for condensation to begin. We have assumed an intermediate value of $\mathcal{S}_{\max} = 10^{-2}$ for iron. This value is our best estimate for the \mathcal{S}_{\max} of vaporous iron based on a knowledge of the maximum supersaturations attained in terrestrial water clouds (Rossow 1978).

The other free parameters of the cloud model are less difficult. The mixing ratios depend on the metallicity, which we have taken to be solar. The chemical equilibrium code requires the metallicity to be specified. Once the assumption of elemental composition is made, however, we can calculate the partial pressures of all the gases in the mixture. We defer a discussion of the effect of brown dwarf metallicity on cloud structure to future work.

The efficiency parameters for coagulation and coalescence, ϵ_{coag} and ϵ_{coal} , are potentially important. However, our model results show that the timescales for these processes, whatever their effi-

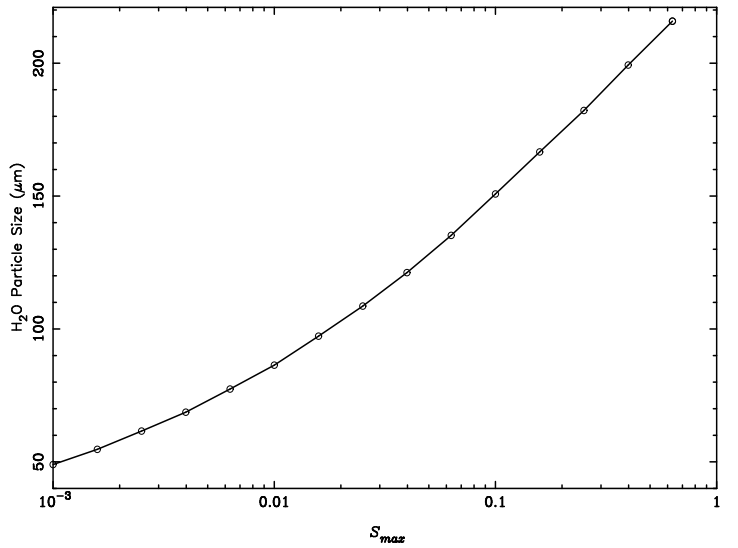


Fig. 6.— The modal particle sizes, as a function of \mathcal{S}_{\max} , for a water cloud in the upper atmosphere of a cool brown dwarf: $T_{\text{eff}} = 350 \text{ K}$ and $g_{\text{surf}} = 10^4 \text{ cm s}^{-2}$. Convection is not occurring in these outer layers. The figure demonstrates the difficulty in estimating particle sizes for radiative (i.e., quiescent) clouds because of the strong dependence of particle size on the assumed maximum supersaturation. Water cloud particles will grow extremely large in a clean atmosphere; i.e., one in which the paucity of condensation nuclei requires high levels of supersaturation of the vapor in order for nucleation to begin. In this case, nucleation proceeds rapidly and the particles grow very large. For convective clouds, on the other hand, the value assumed for the maximum supersaturation is not so important, as the cloud particles will grow to nearly the same size for any value of $\mathcal{S}_{\max} < 100\%$.

ciency, are consistently longer than the timescale of growth by heterogeneous nucleation at 1% supersaturation. The model suggests that coalescence is much faster than coagulation for the two species—iron and water—in which coalescence operates efficiently. The coalescence timescale, for the largest particles we have grown ($\sim 500 \mu\text{m}$), can approach the timescale of heterogeneous nucleation. However, for the clouds in most of the atmospheres we have treated, coalescence is still slower than heterogeneous nucleation by a factor of ten or more. Indeed, unless the efficiency of coalescence is greater than one, requiring charged aerosols (Rossow 1978), coalescence will never dominate particle growth.

4. Comparison With Other Cloud Models

4.1. Ackerman & Marley (2001)

Ackerman & Marley (2001) also employ a one-dimensional cloud model in which cloud layers are treated as horizontally uniform; i.e., in a globally averaged sense. The Ackerman & Marley (2001) cloud model arrives at particle sizes by balancing the upward transport of condensable material due to convective updrafts with the downward sedimentation of condensate. In the case in which the convective timescale, τ_{conv} , dominates over the other growth timescales in the present cloud model, which will occur in vigorously convecting regions of the atmosphere, the results of the present cloud model are expected to produce very similar results to the Ackerman & Marley (2001) treatment. This is because our formulation then reduces to a similar comparison between the characteristic velocities of turbulent convective updrafts and the terminal velocity of particles.

In their treatment of rainout, Ackerman & Marley (2001) introduce an additional parameter, f_{rain} , which characterizes the vertical distribution of condensate in the cloud. The f_{rain} parameter, as Ackerman & Marley (2001) state, is difficult to calculate from basic principles. They leave it as an adjustable parameter in their model. It depends on the mass-weighted sedimentation velocity of the cloud droplets and the convective velocity scale. The difficulty in calculating f_{rain} lies in the complexity of modeling fully the nature of the convection within the cloud. This problem has yet to be successfully attacked for brown dwarf atmo-

spheres.

If it can be computed for these convective clouds, however, knowledge of f_{rain} can potentially provide a more realistic measure of the height and distribution of material in the cloud. For quiescent clouds, f_{rain} does not play a role. Ackerman & Marley (2001) have assumed $f_{\text{rain}} = 2\text{--}3$ in their calculations. The cloud decks they derive are somewhat more compact than those produced in the present cloud model, although both prescriptions lead to rapid depletion of cloud material within a fraction of an atmospheric scale height above the condensation level.

The particle sizes we obtain compare favorably with the sizes predicted by the Ackerman & Marley (2001) model. They predict modal particle radii in the intermediate size range of $40\text{--}80 \mu\text{m}$ for both iron and silicate grains, in good agreement with the particle size ranges shown in Figures 2, 3, and 4.

4.2. Helling *et al.* (2001)

Helling *et al.* (2001) study the onset of cloud particle growth via acoustic waves. They show that small ($1 - 10 \mu\text{m}$ in radius) sized particles can nucleate rapidly, normally within a few seconds. These values are consistent with our particle sizes in radiative regions under the assumption of very low supersaturations ($\mathcal{S}_{\text{max}} \ll 10^{-2}$). Our larger particles form from sustained particle growth by convective uplifting. The grains generated in (Helling *et al.* 2001) are not grown to the maximum size allowed gravitationally, which we assume can occur.

The predictions of the two models in terms of particle radii will be in qualitative agreement in the absence of the τ_{conv} timescale employed in our model. Nevertheless, we emphasize caution in comparing directly the results of these two models. They employ vastly different physical approaches and are therefore not expected to agree in many cases, even qualitatively. The model of Helling *et al.* (2001) attempts a detailed simulation of particle growth in brown dwarf atmospheres, including the complicated effects of hydrodynamics. The goal of the present cloud model, rather, is not to directly simulate the dynamics of particle growth but to develop a computationally economical cloud model that can be incorporated easily

into spectral synthesis models.

5. Discussion

5.1. Cloud Opacity

The effects of clouds on the emergent spectra of substellar objects depend strongly on grain sizes. We derive the wavelength-dependent absorption and scattering opacities of grains with a full Mie theory approach, utilizing the formalism of van de Hulst (1957) and Deirmendjian (1969).

Figure 7 shows the results of such a calculation for forsterite grains in a brown dwarf atmosphere ($T_{\text{eff}} = 1500$ K, $g_{\text{surf}} = 10^5$ cm s $^{-2}$) based on our cloud model results and optical constants from Scott & Duley (1996). Also shown are the results for a larger grain size distribution peaked at $50 \mu\text{m}$, as well as for a size distribution peaked at $0.1 \mu\text{m}$, which is representative of an interstellar particle size (Mathis et al. 1977) often assumed to be appropriate for substellar objects (Allard et al. 2001; Barman et al. 2001). For comparison, we have plotted the atomic and molecular gaseous opacities (Burrows et al. 2001, and references therein) within the cloud region. The substantial absorption and scattering differences between the size distributions, and relative to the gaseous absorption, convey the importance of proper cloud modeling.

5.2. Effect on Spectra

Figure 8 depicts the effects of our modeled forsterite cloud on the emergent spectrum of a brown dwarf ($T_{\text{eff}} = 1500$ K, $g_{\text{surf}} = 10^5$ cm s $^{-2}$). This model atmosphere was obtained using the self-consistent stellar atmosphere code, TLUSTY (Hubeny, I. 1988; Hubeny & Lanz 1995). The base of the forsterite cloud resides at approximately 4 bars and 1800 K, which is the highest temperature in this atmosphere at which forsterite grains can form.

We made two simplifying approximations in producing the cloudy model spectrum shown in Figure 8. First, a cutoff for the cloud deck was desirable to facilitate the calculation of optical depth. We chose this cutoff to be one scale height above the cloud base, which is the atmospheric pressure e-folding distance. Since the remaining cloud-forming material is highly depleted of condensate a

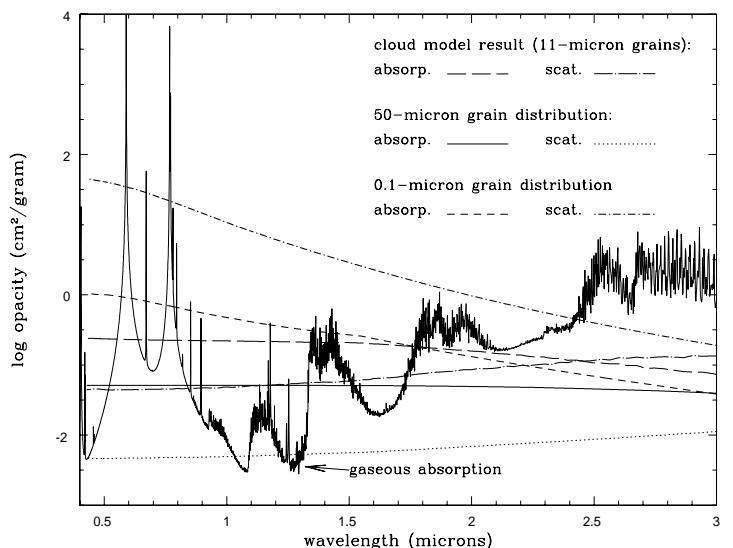


Fig. 7.— Scattering and absorption opacities of forsterite are compared with gaseous atomic and molecular absorption at (1600 K, 2.5 bar). Our modeled modal particle size, $11 \mu\text{m}$, in a brown dwarf ($T_{\text{eff}} = 1500$ K, $g_{\text{surf}} = 10^5$ cm s $^{-2}$) is contrasted with both a larger size distribution peaked at $50 \mu\text{m}$ and a smaller size distribution peaked at $0.1 \mu\text{m}$ (representative of an interstellar grain size assumed by some researchers). In all cases, a functional form of the distribution about the modal size is used (Deirmendjian 1964).

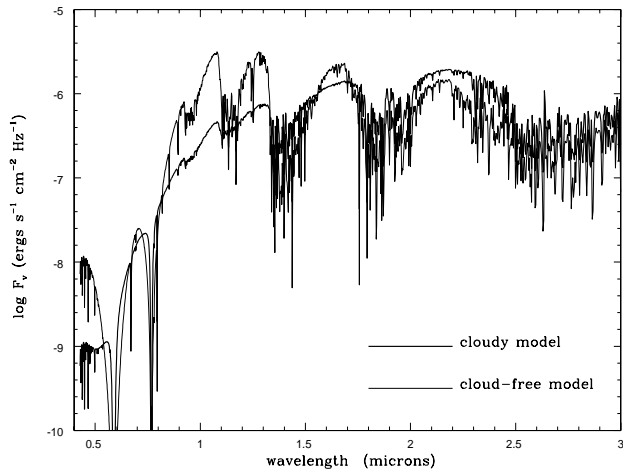


Fig. 8.— The emergent spectrum of a cloudy brown dwarf ($T_{\text{eff}} = 1500$ K, $g_{\text{surf}} = 10^5$ cm s $^{-2}$) is compared with a cloud-free model of the same effective temperature and surface gravity. In the cloudy model, the base of the forsterite cloud resides at approximately 4 bars (1800 K). For the synthetic cloudy spectrum shown, we took the cloud deck to be a scale height thick. This choice will not affect the shape of the model spectrum, however, so long as the cloud deck is more than about a third of a scale height thick, since the cloud is very tenuous and thus optically thin high above the cloud base. The particle size distribution was chosen to be the same throughout the cloud deck for simplicity. We used a Deirmendjian (1964) distribution centered around $11 \mu\text{m}$, which was the typical particle size in the forsterite cloud deck as computed by the cloud model. Within the cloud region, the full solar abundance of magnesium has been condensed into forsterite grains.

scale height above the condensation level (see Section 2.3, Equation 22), the cloud in this region is optically thin. This simplification is therefore not a concern, and the spectral model shown in Figure 8 incorporates the full opacity of the cloud.

Second, owing to difficulties in computing the Mie theory scattering and absorption opacities iteratively, we chose to simplify the radiative transfer problem by using a uniform modal particle radius of $11 \mu\text{m}$ throughout the cloudy region. That is, at every atmospheric pressure level for which we computed the opacity of particles, we employed the Deirmendjian (1964) particle size distribution, given by Equation 23, with value of r_0 equal to $11 \mu\text{m}$. The scattering and absorption opacities of a cloud of $11 \mu\text{m}$ forsterite particles are shown in Figure 7. This value represents the typical particle size in the cloud deck, accounting for the decrease in density of cloud material with height above the cloud base (i.e., a number density weighted average of the particle sizes predicted by the cloud model).

A cloud-free model of the same effective temperature and gravity is plotted for comparison. Within the *B* ($\sim 0.45 \mu\text{m}$) and *Z* ($\sim 1 \mu\text{m}$) bands, the emergent flux is lowered by as much as one dex. However, the strong absorption by the wings of the sodium and potassium resonance lines is mitigated somewhat due to the clouds. Also of interest are the differences in the *J* ($\sim 1.25 \mu\text{m}$), *H* ($\sim 1.6 \mu\text{m}$), and *K* ($\sim 2.2 \mu\text{m}$) infrared bands. The presence of clouds reduces the emergent flux in the otherwise relatively clear *J* and *H* bands, allowing more flux to escape between these bands and at longer wavelengths. In fact, the *J* – *K* colors differ by over 1.5 magnitudes between the cloudy and cloud-free models.

The cloudy spectrum presented in Figure 8 is intended to demonstrate the potential importance of clouds as an opacity source in SMO atmospheres. We defer to future work the problem of more realistically incorporating the opacity of clouds into spectral synthesis models.

5.3. Coupling Clouds With SMO Atmosphere Models

Developing fully self-consistent atmosphere models with clouds is potentially problematic because clouds perturb the radiative balance of the

upper atmosphere. Scattering and absorption of radiation by the cloud causes the temperature–pressure structure of a cloudy atmosphere to deviate from the structure of a cloud–free atmosphere having the same effective temperature and surface gravity. The extent of the effect is strongly dependent on the location of the cloud in the atmosphere and the vertical variation of cloud particle sizes and number densities. Calculating an atmospheric profile that is in radiative equilibrium including both the gaseous opacity and the opacity of the cloud is straightforward. The potential inconsistency arises from the fact that the nature of the cloud itself, including the cloud base location and the particle sizes, depends in general on the temperature–pressure profile of the atmosphere, as we show in Section 2. This is a problem faced by all research groups attempting to include clouds completely self–consistently into SMO spectral synthesis models.

We explored this problem quantitatively by comparing the temperature–pressure profile of two atmosphere models, a “cloudy” model atmosphere and a “cloud–free” model atmosphere, at the same effective temperature and surface gravity. The cloud–free model used for this test was obtained using TLUSTY, our self–consistent model atmosphere code (Hubeny, I. 1988; Hubeny & Lanz 1995), by including only the opacity from gaseous atomic and molecular absorption. We then applied the cloud model described in Section 2 to this cloud–free atmosphere to obtain the distribution of particle sizes and densities of the forsterite cloud predicted to form near the object’s visible surface. For simplicity, we took a sensible average of the particle sizes output by the cloud model and calculated, for a cloud of uniform modal particle size, the absorption and scattering of radiation by the particles using the Mie theory approach outlined in Section 5.1. We then incorporated this opacity back into the atmosphere code to recompute the temperature–pressure structure, thus obtaining the cloudy model atmosphere. We found the cloudy atmosphere to be hotter by several hundred degrees than the cloud–free atmosphere at the same pressure, a significant change. This is the back-warming effect of the cloud alluded to previously.

We then applied the cloud model to the new cloudy atmosphere to see whether the forsterite

grain sizes varied significantly as a result of the change in the temperature–pressure profile. We found that the particles did change in size: their radius increased by about a factor of three. That is, the forsterite cloud looks quite different for the perturbed atmosphere model than it does for the original cloud–free model. This change is a result of the fact that the forsterite cloud straddles the convective–radiative boundary of the atmosphere. Thus, in the original model, the forsterite cloud appears in a convectively stable region of the brown dwarf, but in the perturbed model, the forsterite cloud forms in the convective zone of the atmosphere. Thus, the particles in the perturbed model came out larger than the particles in the original model (Figure 5 shows how particles in radiative regions are systematically smaller than particles forming in convective regions).

We performed a similar test for iron clouds. Unlike for the forsterite cloud, we found only a small change in the particle sizes—a decrease of about 15% in radius—resulting from the perturbation in the atmospheric temperature–pressure structure. The iron cloud forms deeply enough in the convective region of the brown dwarf studied to not be strongly affected by the heating due to the cloud. The degree of inconsistency between cloud–free and cloudy profiles therefore depends on the details of the calculation itself. In many cases, the discrepancies will not be a major concern, but they can be particularly large if the condensation curve happens to intersect the atmospheric profile near the convective–radiative boundary.

We emphasize that both the “cloud–free” and “cloudy” model atmospheres described above satisfy the radiative equilibrium boundary condition, and in that sense, the profiles are self–consistent. The remaining inconsistency arises from not accounting properly for possible adjustments to the opacity of the cloud when the particle sizes change after the profile is perturbed. A future challenge will be developing the machinery to generate model atmospheres that incorporate clouds fully self–consistently.

6. Conclusions

6.1. General Results

We have addressed the condensation and subsequent growth of cloud particles in the atmospheres

of brown dwarfs. We present optimal particle sizes for three abundant species—iron, forsterite, and gehlenite—for a broad range of brown dwarf effective temperatures and surface gravities.

High-gravity brown dwarfs exhibit clouds with typical particle sizes in the $5 - 20 \mu\text{m}$ range. The particles grow much larger, however, in low-gravity objects, often greater than $100 \mu\text{m}$ in radius. We discovered a similar trend with effective temperature: hot brown dwarfs have characteristically larger particle sizes than cool brown dwarfs because of the increased energy flux that must be transported by convection. The distribution of cloud particle sizes depends strongly on the atmospheric parameters, and it is therefore unrealistic in spectral models to assume a single particle size distribution for the entire class of SMOs.

We demonstrate that particle size crucially affects the optical depth of the cloud. Unlike clouds having a particle size distribution centered at $0.1 \mu\text{m}$, these cloud decks do not dominate the opacity. Rather, they smooth the emergent spectrum and partially redistribute the radiative energy (see Figure 8).

6.2. Improved Cloud Models: Morphology and Patchiness

A complete theory of brown dwarf and giant planet atmospheres will require detailed modeling of clouds. Although obtaining plausible particle sizes is a good start, we have been unable to say anything yet about the morphology or patchiness of clouds. For example, on Jupiter, clouds appear in banded structures that vary latitudinally, while Neptune and Uranus show less latitudinal banding in their surface cloud patterns. The structure and patchiness of clouds on brown dwarfs is not known, though the putative variability reported by Bailer-Jones & Mundt (2001) suggests that cloud patches are not necessarily static.

A simple approach to understanding surface cloud distributions is the moist entraining plume model. Such a model has been put forth by Lunine et al. (1989) based on the work of Stoker (1986) for Jupiter’s equatorial plumes. The model generates plumes from atmospheric material whose buoyancy is increased by the release of latent heat from condensation.

More elaborate calculations would involve

three-dimensional modeling of the general atmospheric circulation. Such an approach would be quite difficult to implement, especially without accurate meteorological data for SMO atmospheres. General circulation models would also be too intensive computationally to directly incorporate into SMO spectral models.

6.3. Future Work in Spectral Synthesis

The results of the current work will be useful in developing more elaborate spectral models of substellar atmospheres. We plan to follow up the present work with an exploration of the spectral effects of a variety of cloud compositions and distributions. Although Figure 8 shows the general effects of introducing a forsterite cloud on the spectrum of a brown dwarf, we have not yet varied the particle size distribution from the base to the top of the cloud. A large drop in the particle sizes with height above the cloud base will produce greater optical depth than a cloud deck having uniformly large particles. It is also likely that clouds of more than one species will form near the photosphere simultaneously. A major future challenge of this field will be to model the time dependent dust formation processes of all the major condensable species together, including the possible formation of *core-mantle* grains, which are composed of multiple chemical phases, and then to incorporate them fully self-consistently into substellar model atmospheres.

We thank Ivan Hubeny, Chris Sharp, Jonathan Fortney, Jason Barnes, Adam Showman, Bill Hubbard, Jim Liebert, and the referee for insightful discussions and advice. This work was supported in part by NASA grants NAG5-10450, NAG5-10760 and NAG5-10629.

REFERENCES

- Ackerman, A. S. & Marley, M. S. 2001, *ApJ*, 556, 872
- Allard, F., Hauschildt, P. H., Alexander, D. R., Tamanai, A., & Schweitzer, A. 2001, *ApJ*, 556, 357
- Anders, E. & Grevesse, N. 1989, *Geochim. Cosmochim. Acta*, 53, 197

- Bailer-Jones, C. A. L. & Mundt, R. 2001, *A&A*, 367, 218
- Barman, T. S., Hauschildt, P. H., & Allard, F. 2001, *ApJ*, 556, 885
- Barshay, S. S. & Lewis, J. S. 1976, *ARA&A*, 14, 81
- Basri, G. 2000, *ARA&A*, 38, 485
- Burrows, A., Hubbard, W. B., & Lunine, J. I. 1989, *ApJ*, 345, 939
- Burrows, A., Hubbard, W. B., Lunine, J. I., & Liebert, J. 2001, *Reviews of Modern Physics*, 73, 719
- Burrows, A., Marley, M., Hubbard, W. B., Lunine, J. I., Guillot, T., Saumon, D., Freedman, R., Sudarsky, D., & Sharp, C. 1997, *ApJ*, 491, 856
- Burrows, A. & Sharp, C. M. 1999, *ApJ*, 512, 843
- Deirmendjian, D. 1964, *Applied Optics* (1964)
- . 1969, *Electromagnetic Scattering on Spherical Polydispersions* (New York: American Elsevier Publishing Company, Inc.)
- Helling, C., Oevermann, M., Lüttke, M. J. H., Klein, R., & Sedlmayr, E. 2001, *A&A*, 376, 194
- Hubeny, I. & Lanz, T. 1995, *ApJ*, 439, 875
- Hubeny, I. 1988, *Computer Physics Comm.*, 52, 103
- Jacobson, M. Z. 1999, *Fundamentals of Atmospheric Modeling* (Cambridge, UK: Cambridge University Press)
- Jones, H. R. A. & Tsuji, T. 1997, *ApJ*, 480, L39
- Kirkpatrick, J. D., Reid, I. N., Liebert, J., Cutri, R. M., Nelson, B., Beichman, C. A., Dahn, C. C., Monet, D. G., Gizis, J. E., & Skrutskie, M. F. 1999, *ApJ*, 519, 802
- Landau, L. D. & Lifshitz, E. M. 1959, *Fluid mechanics (Course of theoretical physics)*, Oxford: Pergamon Press, 1959)
- Leggett, S. K., Toomey, D. W., Geballe, T. R., & Brown, R. H. 1999, *ApJ*, 517, L139
- Lewis, J. S. 1969, *Icarus*, 10, 365
- Lide, D. R. 1991, *CRC Handbook of chemistry and physics. A ready-reference book of chemical and physical data* (Boca Raton: CRC Press, 1991/92, 72nd ed., edited by Lide, David R.)
- Lunine, J. I., Hubbard, W. B., Burrows, A., Wang, Y.-P., & Garlow, K. 1989, *ApJ*, 338, 314
- Mathis, J. S., Rimpl, W., & Nordsieck, K. H. 1977, *ApJ*, 217, 425
- Rogers, R. R. & Yau, M. K. 1989, *A Short Course in Cloud Physics* (Butterworth-Heinemann, 1989)
- Rossow, W. B. 1978, *Icarus*, 36, 1
- Scott, A. & Duley, W. W. 1996, *ApJS*, 105, 401
- Stevenson, D. J. & Lunine, J. I. 1988, *Icarus*, 75, 146
- Stoker, C. R. 1986, *Icarus*, 67, 106
- Sudarsky, D., Burrows, A., & Pinto, P. 2000, *ApJ*, 538, 885
- Tokano, T., Neubauer, F. M., Laube, M., & McKay, C. P. 2001, *Icarus*, 153, 130
- van de Hulst, H. C. 1957, *Light Scattering by Small Particles* (New York: John Wiley & Sons, 1957)
- Woitke, P. 1999, in *Astronomy with Radioactivities*, 163–+

This 2-column preprint was prepared with the AAS L^AT_EX macros v5.0.